www.advsustainsys.com

# Exploring PANI/CBTS Nanofiber Composites as Supercapacitor Electrodes: Structure—Performance Correlation

Süleyman Gökhan Çolak,\* Ahmet Güngör,\* Melis Özge Alaş Çolak, Utku Bulut Simsek, Rukan Genc. and Emre Erdem

In this study, the electrochemical performance of supercapacitors is investigated using nanofiber Polyaniline (PANI) and PANI/Cu<sub>2</sub>BaSnS<sub>4</sub> (CBTS) composites with CBTS concentrations of 5%, 10%, and 20%. BET surface area and Horvath-Kawazoe (HK) pore volume analyses show that nanofiber PANI has a higher surface area (35.3 m<sup>2</sup> g<sup>-1</sup>) and pore volume (0.1391 cm<sup>3</sup> g<sup>-1</sup>) compared to CBTS (2.2 m<sup>2</sup> g<sup>-1</sup> and 0.0107 cm<sup>3</sup> g<sup>-1</sup>). Adding CBTS to PANI reduces these values, with composites ranging from 22.82 to 24.35 m<sup>2</sup> g<sup>-1</sup> and 0.1654 to 0.1845 cm<sup>3</sup> g<sup>-1</sup>, respectively. HRTEM reveals evenly dispersed PANI nanofibers (40-60 nm diameter, several micrometers long), with CBTS crystalline regions (12-26 nm) on PANI/CBTS5, enhancing electrical conductivity. XPS confirms CBTS doping and significant electronic interactions between PANI and CBTS, detailing the chemical states of Cu, Ba, Sn, and S. Electrochemical tests over 10000 cycles demonstrate that PANI/CBTS composites outperform pure PANI, with PANI/CBTS5 achieving a specific capacitance of 374.2 F g<sup>-1</sup> and an energy density of 5.20 Wh kg<sup>-1</sup>. Higher CBTS concentrations slightly lower the specific capacitance. This pioneering study of CBTS's synergistic effects in supercapacitors highlights the potential of PANI/CBTS composites as promising materials for advanced energy storage applications.

#### 1. Introduction

Supercapacitors have garnered significant interest in electrical energy storage owing to their remarkable power densities, extended operational lifespans, rapid charge/discharge rates, and broad temperature working ranges. [1,2] Intensive research is being concentrated on using diverse materials and composite architectures in supercapacitors to improve energy storage efficacy. [3,4]

Currently, intensive research is focused on using various materials and composite structures in supercapacitors to enhance energy storage performance. Chalcogenide transition metal sulfide materials are being actively investigated and used as potential electrode materials in energy storage technologies. [5,6] Studies have explored the use of chalcogenides such as Cu<sub>2</sub>ZnSnS<sub>4</sub>/PANI, [6] Cu<sub>2</sub>NiSnS<sub>4</sub>/rGO, [7] Cu<sub>2</sub>CoSnS<sub>4</sub>, [8] and Cu<sub>2</sub>FeSnS<sub>4</sub>/PVP/rGO. [9] In

S. G. Çolak
Department of Biomedical Engineering
Faculty of Engineering and Natural Sciences
Iskenderun Technical University
Hatay 31200, Turkey

E-mail: sgokhan.colak@iste.edu.tr

A. Güngör, E. Erdem Faculty of Engineering and Natural Sciences Sabanci University Istanbul TR-34956, Turkey

E-mail: ahmet.gungor@sabanciuniv.edu

The ORCID identification number(s) for the author(s) of this article can be found under https://doi.org/10.1002/adsu.202500427

© 2025 The Author(s). Advanced Sustainable Systems published by Wiley-VCH GmbH. This is an open access article under the terms of the Creative Commons Attribution License, which permits use, distribution and reproduction in any medium, provided the original work is properly cited

DOI: 10.1002/adsu.202500427

M. Ö. Alaş Çolak, R. Genc SUNUM Nanotechnology Research Centre Sabanci University Istanbul TR-34956, Turkey

U. B. Simsek Department of Machine Istanbul Aydin University Anadolu BIL Vocational School Istanbul TR-34295, Turkey

M. Ö. Alaş Çolak, R. Genc Department of Chemical Engineering

Faculty of Engineering
Mersin University

Mersin 33343, Turkey A. Güngör, E. Erdem

Center of Excellence for Functional Surfaces and Interfaces for

Nano-Diagnostics (EFSUN) Sabancı University

Orhanlı, Tuzla, Istanbul TR-34956, Turkey

U. B. Simsek department of Machine Anadolu BIL Vocational School Istanbul Aydin University 34295, Turkey www.advancedsciencenews.com



www.advsustainsys.com

supercapacitor applications alongside nanomaterials like 2D graphene, graphene oxide (GO), reduced graphene oxide (rGO), and polyaniline (PANI). Among chalcogenide materials, copperbased barium tin sulfide Cu<sub>2</sub>BaSnS<sub>4</sub> (CBTS) stands out due to its significant surface area, chemical and thermal stability, conductivity, good optoelectronic properties, cost-effectiveness, abundance in nature, and non-toxicity.[10,11] These properties make CBTS a promising candidate for applications such as photovoltaic solar cells and energy storage devices.[10-12] Moreover, its optimized surface properties may enhance its electrochemical utilization, making it suitable for energy storage devices. The potential of CBTS as electrodes in supercapacitors remains underutilized and largely unexplored. To further situate our work within the field, it is worth noting that organic-inorganic hybrid composites organic-inorganic hybrid composites, which integrate the electronic conductivity and mechanical flexibility of polymers with the structural robustness and redox activity of inorganic frameworks, have emerged as a promising class of electrode materials for supercapacitors. For instance, Liu et al. demonstrated enhanced cycling stability and a capacitance of 325 F g-1 in polyaniline-titanate hybrids.[13] Similarly, Chen et al. reported that PANI-Zn-MOF composites achieved high energy densities owing to efficient charge transport at the organic-inorganic interface.[14] These studies underscore the potential of combining conductive polymers with chalcogenide nanostructures, motivating our exploration of PANI/CBTS systems.

Conductive polymer refers to a type of polymer that is inherently electrically conductive without requiring external additives or processing.[15,16] These polymers are unique in that they possess inherent electronic properties, enabling the movement of charge carriers due to specific chemical structures within the polymer backbone. Due to the presence of a conjugated  $\pi$ -electron backbone, conductive polymers have been considered reliable and pseudocapacitor electrode materials, thanks to their unique electronic properties, such as low-energy optical transmission, low ionization potential, and high electron affinities.[15,16] Various conductive polymers such as PANI, polypyrrole (PPy), and polythiophene (PTh) are commonly used electrode materials for supercapacitor applications. PANI can be polymerized using various techniques with aniline monomer and offers several advantages due to its ease of preparation, facile acid-base chemistry, and ecological sustainability.[17,18] It has become one of the most efficient materials for supercapacitor electrodes due to its superior electrical conductivity, affordable cost, high pseudo-capacitance behavior, and rapid doping/doping during charge-discharge.[19,20] However, PANI's morphological and mechanical properties result in a low charge transfer rate and significant swelling/shrinkage during continuous charge/discharge, leading to a low specific capacitance, poor rate capability, and minimal cyclic stability. [20,21] Therefore, to create supercapacitors with high power and energy density, PANI is often used as an additive or in composite form with other electrodes like carbon materials, metal oxides, metal-organic frameworks, and/or CZTS materials.[5,22,23] In our previous study, we synthesized PANI/CZTS nanocomposites using the in situ chemical oxidative polymerization method. We employed them as electrodes to synergistically enhance the electrochemical performance of both symmetric and asymmetric supercapacitors.<sup>[24]</sup> Combining PANI with CZTS significantly enhanced the specific capacitance, energy density, and power density values. In the asymmetric supercapacitor device, the specific capacitance, energy density, and power density were 311 F g $^{-1}$ , 43.2 Wh kg $^{-1}$ , and 440 kW kg $^{-1}$ , respectively, and showed significantly improved values. [6]

With the increasing importance of supercapacitors in energy storage, developing new materials that provide higher performance and longer life is of great importance. The combination of the large surface area and chemical/thermal stability of CBTS with the high conductivity and environmentally benign nature of PANI offers a promising alternative for developing supercapacitors. In summary, this work aims to create a novel nanocomposite material by leveraging the unique properties of CBTS and PANI to enhance the performance of supercapacitors. In this direction, nanocomposites containing CBTS and PANI in varying amounts (5%, 10%, and 20% by mass) were synthesized, and their physical, chemical, structural, and surface morphological properties were characterized using FT-IR, FE-SEM, XRD, and Raman. Electrochemical characterizations of the supercapacitor performance of the produced PANI/CBTS nanocomposite materials were carried out using cyclic voltammetry (CV), potentiostatic electrochemical impedance spectroscopy (PEIS), and potential-limited galvanostatic cycling (GCPL) techniques.

## 2. Experimental Section

## 2.1. Materials

All compounds employed in the manufacture of the materials were used without purification. Copper chloride (CuCl<sub>2</sub>) (Sigma–Aldrich), Barium sulphate (BaSO<sub>4</sub>) (Across Organics), Tin chloride (SnCl<sub>4</sub>) (TCI Chemical), and Thiourea (CS(NH<sub>2</sub>)<sub>2</sub>) (Across Organics) were purchased from commercial sources. Aniline hydrochloride (Thermo-scientific, purity: 99%) functioned as the monomer, while ammonium persulfate (Acros Organics APS, purity: 98+%) was utilized as the initiator. Sulfuric acid (95–98 wt.%) was used as the solvent, obtained from Sigma–Aldrich. Water employed throughout the synthesis underwent purification using a Millipore Milli-Q system (Millipore Inc.,  $\Omega = 18 \text{ M}\Omega \text{ cm}$ ).

#### 2.2. Synthesis of CBTS

CBTS was produced utilizing a solution-based conventional synthesis process reported in our previous work. [6] The precursor solution was prepared by dissolving, in a molar ratio of 2:1:1:8, CuCl<sub>2</sub>, BaSO<sub>4</sub>, SnCl<sub>4</sub>, and (CS(NH<sub>2</sub>)<sub>2</sub>) in a mixed ethylene glycol solvent system. Subsequently, the solution placed within the stainless steel underwent heat treatment in a controlled environment at 200 °C to facilitate the formation of the essential kesterite phase. The final product was refined by washing times with ethanol and water, providing a black solid powder. [25–27]

### 2.3. Synthesis of PANI

Aniline monomer (1 mmol) was dissolved in 10 mL of 1 M perchloric acid ( $HClO_4$ ) solution and stirred for 10 min. In a separate beaker, ammonium persulfate (APS) (1 mmol) was added

onditions) on Wiley Online Library for rules of use; OA articles are governed by the applicable Creative Commons License

Scheme 1. Represented synthesis of PANI, CBTS, and PANI/CBTS nanocomposites.

to 100 mL of 1 M HClO $_4$  and stirred for 10 min until fully dissolved. The APS solution was then slowly added dropwise to the aniline solution under constant stirring at room temperature for 10 min. The solution turning dark green indicated the initiation of the polymerization reaction. The reaction mixture was cooled to 4 °C and allowed to react for 24 h to yield pure PANI. The resulting product was collected via centrifugation, washed with ethanol and deionized water, and dried at 70 °C for 24 h.[28]

#### 2.4. Synthesis of PANI/CBTS Nanocomposites

To synthesize PANI: CBTS nanocomposites with varying compositions (5%, 10%, and 20% CBTS by mass (w/w,%)), the procedure described above was followed with slight modifications. CBTS powder was added to a beaker containing 10 mL of 1 M  $\rm HClO_4$  and stirred using a magnetic stirrer for 30 min to ensure homogeneity. Subsequently, the aniline solution prepared separately was added to the CBTS solution, and the polymerization reaction was carried out following the same steps as in the synthesis of pure PANI. The resulting nanocomposites were labelled as PANI, PANI:CBTS5, PANI:CBTS10, and PANI:CBTS20, corresponding to the respective compositions of the nanocomposites (Scheme 1).

#### 2.5. Characterizations of Synthesized Nanocomposites

Various analytical techniques were employed to characterize the chemical and surface properties of both the synthesized CBTS and PANI/CBTS nanocomposite materials. Fourier transform infrared (FT–IR) spectroscopy, conducted using a Thermo Scientific iS50 apparatus, covered a spectral range from 4000 to 1000 cm<sup>-1</sup>. This method provided insights into the molecular bonding and transmittance characteristics of the nanocomposites. Surface morphology was examined utilizing a Jeol JEM-ARM200CFEG high-resolution transmission electron microscope (HRTEM) and a Zeiss Supra 55 Field Emission scanning electron microscope

(FESEM). Images were captured at magnifications of 100 and 200 kx, corresponding to scales of 100 and 200 nm, respectively, with an accelerating voltage of 15 kV. X-ray Photoelectron Spectroscopy (XPS) analysis was performed using a Thermo Scientific K-Alpha X-ray Photoelectron Spectrometer, which features a 180° hemispherical analyzer, an Al Kα micro-focused monochromator, and a variable spot size (30-400 µm). It features an ion gun (100–4000 eV), dual-beam charge compensation, and a 60  $\times$ 60 mm sample stage. Data acquisition used Avantage software. Raman spectroscopy analysis was performed using a Renishaw InVia Qontor system, covering a wavelength range of 200-2000 cm<sup>-1</sup>, with laser excitation at 785 and 532 nm at ambient temperature. The instrument utilized an upright microscope and a frequency-doubled Nd:YAG laser to generate a 1-µm-diameter spot on the sample surface. X-ray diffraction (XRD) analysis was conducted using a Bruker D2 Phaser instrument, scanning the  $2\theta$  angle from 10° to 90° at a rate of 1° min<sup>-1</sup>. The XRD utilized an X-ray wavelength of 1.540 Å, operating at 30 kV voltage and 10 mA current. Samples were prepared in powder form for analysis.

The energy density and power density of the manufactured electrodes have been determined using Equations (2) and (3), respectively. Where  $\Delta V$  (V) is the maximum potential window and  $\Delta t$  (s) is the discharging time.

Specific Capacitance 
$$(C_s) = \frac{\int_{V_1}^{V_2} I(V) dV}{2mv\Delta V}$$
 (1)

Energy Density, 
$$E = \frac{0.5 * C_s * \Delta V^2}{3.6}$$
 (2)

Power Density, 
$$P = \frac{E}{(\Delta t/3600)}$$
 (3)

Supercapacitor performance was evaluated using various analytical techniques, including potential electrochemical impedance spectroscopy (PEIS), cyclic voltammetry (CV), and galvanostatic charge/discharge (GCPL). The electrodes were fabricated using the PANI and PANI/CBTS nanocomposites

of use; OA articles are governed by the applicable Creative Commons I

**Table 1.** The specific supercapacitor designs are based on the synthesized nanocomposites.

Sample	Electrode 1	Electrode 2	Electrolyte	Separator	Туре
PANI	PANI	PANI	3 M KOH	Glass fiber	Symmetric
PANI/CBTS5	PANI/CBTS5	PANI/CBTS5	3 M KOH	Glass fiber	Symmetric
PANI/CBTS10	PANI/CBTS10	PANI/CBTS10	3 M KOH	Glass fiber	Symmetric
PANI/CBTS20	PANI/CBTS20	PANI/CBTS20	3 M KOH	Glass fiber	Symmetric

that were created. The investigations were carried out using a voltage range of 0–1V, with 3M KOH serving as the electrolyte for the experiments (Table 1 and Scheme 2). The impedance testing of the supercapacitors was performed across a broad frequency spectrum ranging from 1 mHz to 10 MHz. The CV was examined using an extensive scanning rate (1–200 mV s $^{-1}$ ), including high and low scanning rates. The GCPL test quantified different current densities, ranging from 0.1 to 2.4 A g $^{-1}$ .

#### 2.6. Dunn's Method

The electrochemical performance of the symmetric device fabricated using PANI and PANI/CBTS composites has been further evaluated through the application of the power law.<sup>[29]</sup> For the analysis, CV tests were performed at scan rates of 1, 3, 5, 7, and 10 mV s<sup>-1</sup>. This specific scan rate was selected based on considerations such as low ohmic resistance and inductance, as well as the optimal electrochemical properties identified in previous analyses. The power law (Equation 4) is expressed as follows:

$$i(v) = av^b (4)$$

where *i* represents the current density (A  $g^{-1}$ ),  $\nu$  denotes the scan rate (mV  $s^{-1}$ ), and b is a constant. The value of b plays a crucial

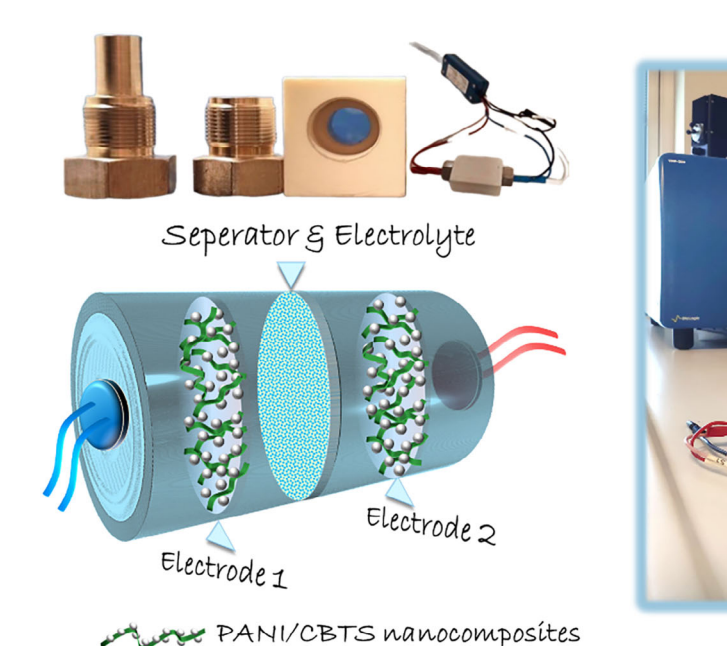
role in determining the charge storage mechanism of the device: b value closer to 1 signifies behavior characteristic of an electric double-layer capacitor (EDLC), where a charge is stored electrochemically through the reversible adsorption of ions in the electrolyte, while b value closer to 0.5 indicates battery-like behavior, where a charge is stored via redox reactions. [30–32] The value of b can be calculated by taking the logarithm of Equation (5) as shown below:

$$\log(i(v)) = \log(k) + b\log(v) \tag{5}$$

#### 3. Results and Discussion

### 3.1. PANI/ CBTS Nanocomposites

PANI exhibits remarkable redox characteristics and the ability to recycle via protonation, allowing it to transition between different oxidation states, including leucoemeraldine base (LB), emeraldine base (EB), and pernigraniline base (PB). These oxidation states are pivotal in PANI's redox processes, influencing its electrical and chemical properties.<sup>[33]</sup> The protonation of EB to form the electrically conductive emeraldine salt (ES) accelerates PANI's redox reactions, facilitating the synthesis of semiquinone segments through protonation at the imine nitrogen atoms.<sup>[34]</sup>



Scheme 2. Represent schematic illustration and two-electrode system measurement of the supercapacitor device.

.com/doi/10.1002/adsu.202500427 by Turkey Cochrane Evidence Aid, Wiley Online Library on [02/12/2025]. See the Terms and Conditions (https://onlinelibrary.wiley.com/terms

and-conditions) on Wiley Online Library for rules of use; OA articles are governed by the applicable Creative Commons

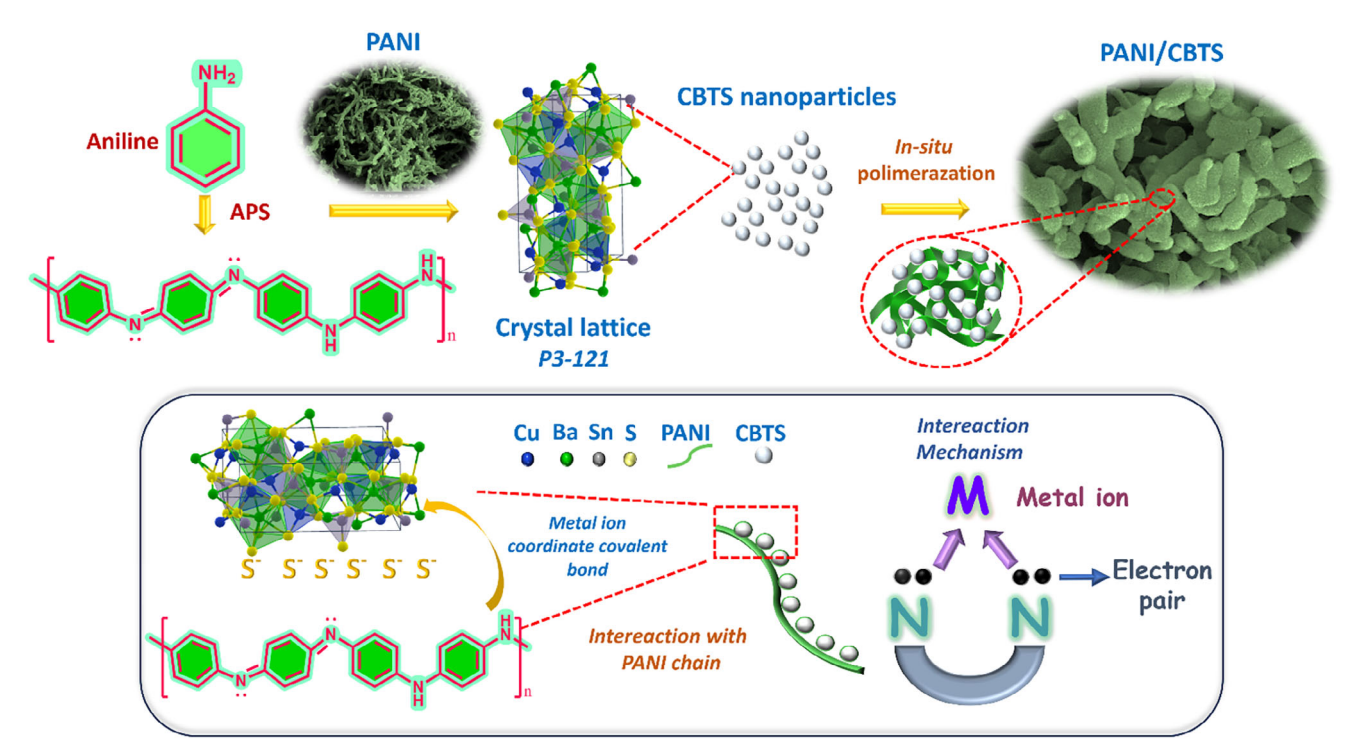


Figure 1. The representation illustrates the creation mechanism of PANI/CBTS nanocomposites.

Additionally,<sup>[35,36]</sup> the mechanism underlying the formation of PANI/CBTS nanocomposites involves the active participation of amine groups (—NH<sub>2</sub>) in PANI. These groups are highly reactive and known for their ability to interact with metal surfaces, forming coordination bonds.<sup>[37,38]</sup> Thus, chemical interactions between PANI and metallic semiconductor materials, such as CBTS, are feasible. The interaction between metal ions (Cu, Ba, Sn, S) on CBTS and PANI occurs due to the amine groups on PANI, which can donate electron pairs to metal ions, forming coordination bonds.<sup>[39]</sup>

This results in a strong chemical bond (C-S-H, Figure 6b) between PANI molecules and the CBTS surface, influencing the physical and mechanical properties of the nanocomposites (Figure 1). These chemical interactions can enhance mechanical strength and optimize material performance. Understanding these mechanisms is essential for tailoring PANI/CBTS nanocomposites for various applications without revealing their origins. The discovery of robust chemical interactions between PANI molecules and the CBTS surface presents promising opportunities for utilizing them in supercapacitors, where PANI/CBTS nanocomposites can serve as electrode materials. The enhanced dispersion of PANI inside the CBTS matrix, aided by these chemical interactions (C—SO<sub>2</sub>—C sulphone, C—S—S—C organic disulfides, and C-S-H thiol (Figure 6b), increases the available surface area and promotes quicker transmission of electric charge. This results in increased specific capacitance and enhanced energy storage capacity, which are vital variables in the performance of supercapacitors. Furthermore, the presence of coordination bonds between PANI and metal ions on the CBTS surface guarantees the extended lifespan of the electrode materials, which is crucial for the dependable performance of supercapacitor devices throughout many charge–discharge cycles. [6]

The FTIR spectrum of PANI presented in Figure 2a reveals several distinctive peaks, each corresponding to specific chemical vibrations that provide vital information on PANI's molecular characteristics and the material's prospective uses.<sup>[40]</sup> The peak at 3397 and 3207 cm<sup>-1</sup> in Figure 2a corresponds to the  $\delta$ (N—H) interatomic tension vibration of PANI. The peak at 1532 cm<sup>-1</sup> represents the C=C stretching vibration of the quinonoid ring of the polymer, whereas the peak at 1410 cm<sup>-1</sup> corresponds to the C=C stretching vibration of the benzenoid ring.<sup>[41]</sup> The peak at 1207 cm<sup>-1</sup> corresponds to the C-N transverse vibration and shows the creation of the emeraldine salt phase of PANI. This stresses the many chemical states and structural polymorphisms of PANI. Other peaks detected in the FTIR spectra of PANI include 1070 and 745 cm<sup>-1</sup>. [42] These peaks indicate the presence of sulfonate groups from APS linked to aromatic rings, as well as aromatic C-H outer plane bending vibrations. These vibrational modes give information on the improved proton conductivity and complicated molecular architecture of PANI.[43] Furthermore, the C-C bond stretching vibrations found in the area between 1410 and 1794 cm<sup>-1</sup> suggest the existence of the emeraldine form of PANI.[44] These vibrations suggest the existence of benzoid and quinoid units typical of the synthesized PANI. The doping of CBTS material into PANI/CBTS5, PANI/CBTS10, and PANI/CBTS20 nanocomposite materials made the typical benzoid and quinoid peaks more conspicuous. The faint vibrational bands detected at 2351 cm<sup>-1</sup> suggest S-H vibrations in CBTS nanoparticles in PANI samples. In contrast, the significant peaks between 1020 and 1420 cm<sup>-1</sup> reflect C-C and C-H bending

23667486, 2025, 10, Downloaded from https://advancec

onlinelibrary.wiley.com/doi/10.1002/adsu.202500427 by Turkey Cochrane Evidence Aid, Wiley Online Library on [02/12/2025]. See the Terms

on Wiley Online Library for rules of use; OA articles are governed by the applicable Creative Commons License

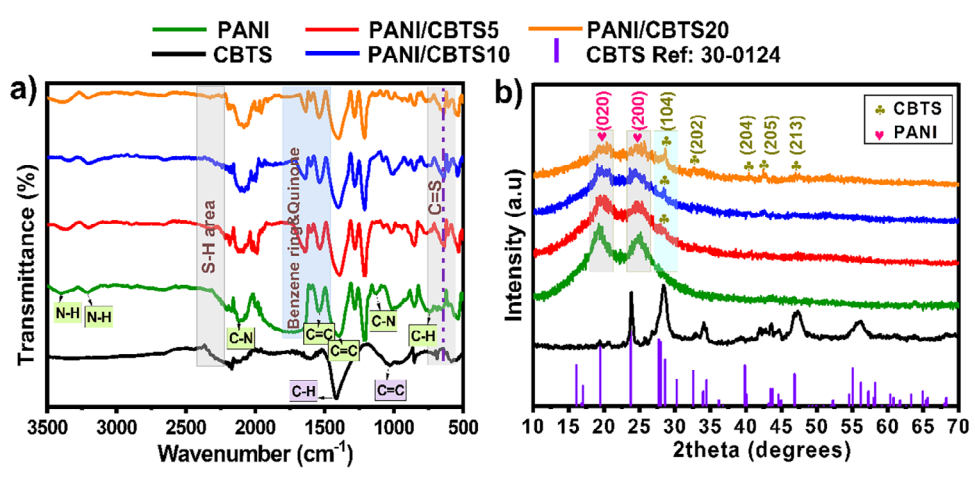


Figure 2. a) FTIR spectrum and b) XRD spectra of CBTS, PANI, PANI/CBTS5, PANI/CBTS10, and PANI/CBTS20 nanocomposites, respectively.

vibrations, and the weak band  $\approx$ 710 cm $^{-1}$  reflects C double bonds and C=S bonds. $^{[6]}$ 

The CBTS material was prepared without sulphuration and was observed to have a P3-121 ( $a=6.36^{\circ}$ ,  $b=6.36^{\circ}$ ,  $c=15.82^{\circ}$ ) crystal lattice. This crystal lattice indicates a specific atomic arrangement within its structure. The lattice exhibits certain symmetry properties and potential deformations, contributing to its unique characteristics. During XRD analysis, a shift of the (112) peak, a characteristic peak of quaternary kesterite crystal

structures, to a lower angle was observed, accompanied by the appearance of additional peaks at  $2\theta = 27.62^{\circ}$  and  $27.97^{\circ}$ . These extra peaks were attributed to the (104) and (110) planes of the tetragonal CBTS (JCPDS card no.: 30-0124). The intensity and width of these peaks provide insights into the crystalline quality of the material. Moreover, the peaks at  $2\theta = 19.35^{\circ}$ ,  $28.62^{\circ}$ ,  $32.62^{\circ}$ ,  $33.91^{\circ}$ ,  $34.38^{\circ}$ ,  $43.50^{\circ}$ ,  $43.82^{\circ}$ ,  $46.79^{\circ}$ ,  $55.11^{\circ}$ ,  $56.24^{\circ}$ , and  $57.18^{\circ}$  agree with the JCPDS card number and reflect the crystalline structural features of CBTS<sup>[26]</sup> (Figure 2b). The distribution

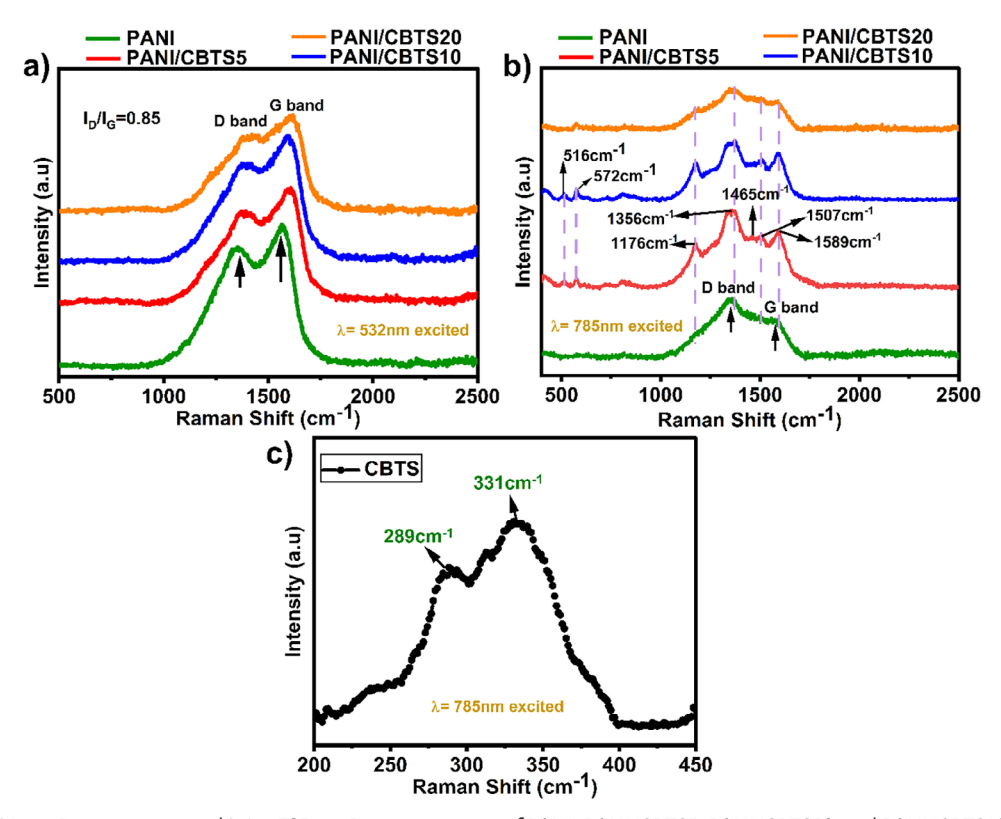


Figure 3. a)  $\lambda = 532$  nm Raman spectrum, b)  $\lambda = 785$  nm Raman spectrum of PANI, PANI/CBTS5, PANI/CBTS10, and PANI/CBTS20 nanocomposites, respectively, and c)  $\lambda = 785$  nm Raman spectrum of CBTS.

23667486, 2025, 10, Downloaded from https://advanced.onlinelibrary.wiley.com/doi/10.1002/adsu.202500427 by Turkey Cochrane Evidence Aid, Wiley Online Library on [02/12/2025]. See the Terms

and-conditions) on Wiley Online Library for rules of use; OA articles are governed by the applicable Creative Commons

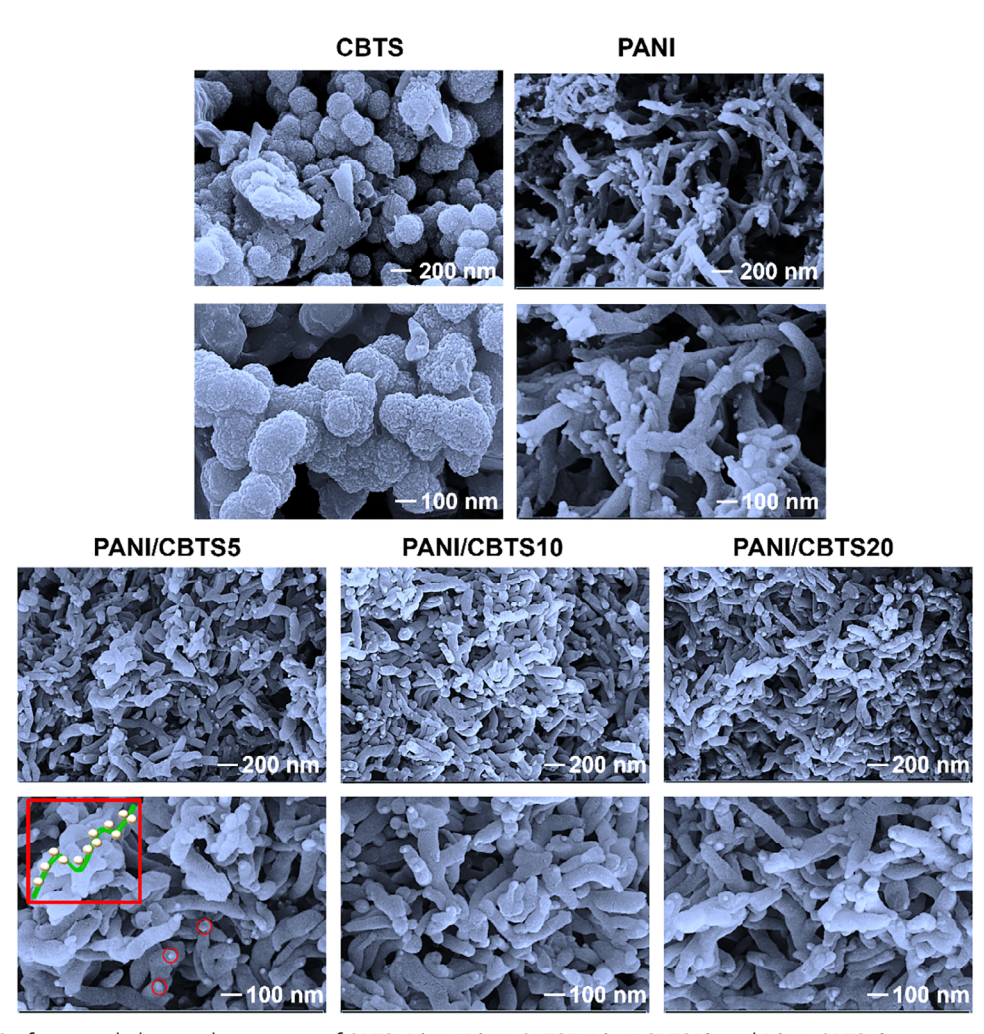


Figure 4. FE-SEM Surface morphology analysis images of CBTS, PANI, PANI/CBTS5, PANI/CBTS10, and PANI/CBTS20 nanocomposites, respectively. (Up: 100.000x mag. Down: 200.000x mag.).

of these peaks further confirms the crystallographic properties of the material and its phase purity. In the XRD analysis of PANI material, two characteristic broad-shouldered peaks at 19.35° and 25.11° were observed, indicating the presence of a polymer structure. [43] The intensity and shape of these peaks provide information about the crystalline nature and molecular arrangement within the polymer matrix.

Additionally, during the XRD analysis of PANI/CBTS5, PANI/CBTS10, and PANI/CBTS20 nanocomposite materials formed by doping CBTS with different percentages, no clear CBTS peaks were observed due to the dominance of PANI materials over CBTS. However, it was determined that a small CBTS peak was observed at 28.63° in the PANI/CBTS20 nanocomposite material, suggesting the presence of CBTS within the nanocomposite structure. All these findings provide important information about the crystal structures and components of the materials and will be further investigated in conjunction with other characterization techniques, such as Raman spectroscopy analysis.

The Raman spectroscopy investigation of PANI/CBTS nanocomposites was conducted at two distinct wavelengths ( $\lambda$  = 532, 785 nm) to explore their structural characteristics and

compositional integrity, with a specific focus on the vibrations between C, H, and N atoms. Excitation at  $\lambda = 785$  nm led to the discovery of two strong peaks at 289 and 331 cm<sup>-1</sup>, matching the distinctive vibrations of CBTS in Figure 3c.<sup>[26]</sup> These peaks support the quaternary chalcogenide structure of the material, reinforcing the structural consistency and purity of the produced nanocomposites. This finding is in accord with prior Raman spectra of single-phase CBTS, further supporting the dependability of the synthesized materials. [49] Upon excitation at  $\lambda =$ 785 nm, the Raman spectra of PANI/CBTS5 and PANI/CBTS10 samples indicated unique interatomic vibrations of PANI polymer (Figure 3b). Specifically, vibrations associated with the C-C benzenoid ring (1589 cm<sup>-1</sup>), C=N imine (1465 cm<sup>-1</sup>),  $\delta$ (N-H) semi-quinoid ring (1564cm<sup>-1</sup>),  $\delta$ (N-H) semi-quinoid ring (1165 cm<sup>-1</sup>), and  $\delta$ (C–H) benzenoid ring (516–572 cm<sup>-1</sup>) were seen.<sup>[46]</sup> Furthermore, the excitation of the PANI structures at  $\lambda = 532$  nm resulted in the development of the D band at 1356 cm<sup>-1</sup> and the G band at 1589 cm<sup>-1</sup>, which serve as crucial markers of the structural features of the polymer<sup>[42]</sup> (Figure 3a).

The G band, attributable to crystal ordering, exhibited a higher wavenumber (1589 cm-1), indicating a more structured

2366/486, 2025, 10, Downloaded from https://datvanced.onlinelibrary.wiley.com/doi/10.1002/ads20.20509027 by Turkey Cochrane Evidence Aid, Wiley Online Library on [02/12/2025]. See the Terms and Conditions (https://onlinelibrary.wiley.com/rems-and-conditions) on Wiley Online Library for rules

of use; OA articles

are governed by the applicable Creative Commons

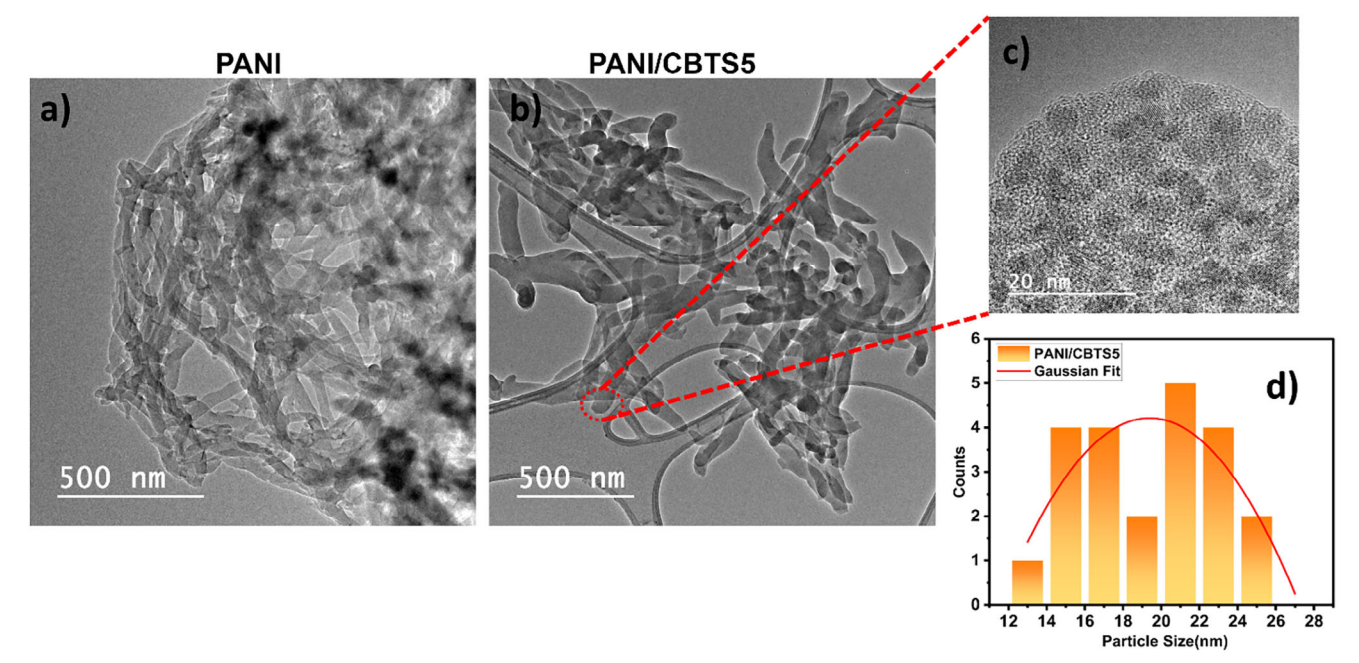


Figure 5. HRTEM analysis images of PANI nanofiber (a), PANI/CBTS5 (b, c) nanofiber composite, and particle size distribution of PANI/CBTS5 nanofiber composites.

molecular arrangement within the PANI chains. Conversely, the existence of the D band at 1356 cm $^{-1}$  showed structural weaknesses or faults inside the PANI, possibly influencing the overall characteristics and use of the material. The computed  $\rm I_D/I_G$  ratio of 0.85, below 1, suggests a relatively low degree of crystal disorder, further verifying the structural integrity of the PANI/CBTS nanocomposites. Although the D and G band values presented here differ significantly from those reported in the original work, the interpretation of the results obtained by Raman spectroscopy is consistent with the structural analysis of PANI/CBTS nanocomposites. In conclusion, the observed vibrational modes and band intensities give vital information on the molecular order and structural quality of the produced nanocomposite materials.

**Figure 4** thoroughly analyses the surface morphology of CBTS, PANI, PANI/CBTS5, PANI/CBTS10, and PANI/CBTS20 nanomaterials. The dispersion of all samples was uniform across the surface. The SEM scans revealed that the surface morphology of CBTS exhibited a cauliflower-like shape. [50] PANI, in contrast, exhibits a surface morphology resembling nano-sized structures, with a thickness that spans within the range of 80–90 nm. The nanostructures were observed at dimensions of 100 and 200 nm.

By affecting intra- and inter-chain interactions, CBTS doping can cause morphological changes in PANI. By linking CBTS to the —N atoms in the imine group rather than the chain ends, a more condensed morphological structure was achieved. [39] Consequently, as the amount of CBTS increased, the thickness of PANI in the structure also increased, leading to a partial reduction in its porosity. This situation is also consistent with the BET surface area results (refer to Table 2). The surface area of the BET decreases as the concentration of CBTS increases.

HRTEM images reveal the structural and morphological features of the investigated samples of PANI and PANI/CBTS5. The images show that PANI nanofibers have a homogeneous distribution, with diameters ranging from ≈40 to 60 nm. The lengths of the nanofibers reach several micrometers, indicating that PANI has a high surface area and may be suitable for supercapacitor applications. Furthermore, TEM images reveal the presence of regular CBTS crystalline regions on the surface of PANI/CBTS5 nanofibers. These crystalline regions may enhance the electrical conductivity properties of PANI. The CBTS crystals have an average diameter of 12–26 nm and are uniformly distributed, as shown in the histogram plot (Figure 5d). This structure can improve the electrical conductivity performance of

Table 2. BET surface area and Horvath-Kawazoe (HK) cumulative PANI and CBTS nanocomposite pore volume.

Material	BET surface area [m <sup>2</sup> g <sup>-1</sup> ]	HK Cumulative Pore Volume [cm $^3$ g $^{-1}$ ]		
PANI	35.3	0.1391		
CBTS	2.2	0.0107		
PANI/CBTS5	24.3	0.1845		
PANI/CBTS10	24.1	0.1654		
PANI/CBTS20	22.8	0.1734		



www.advancedsciencenews.com



www.advsustainsys.com

the composite material. The images also show that PANI and CBTS particles formed aggregates in some regions, which are thought to be caused by dissolution problems of the sample prepared for analysis. The distribution of CBTS particles on PANI nanofibers is depicted in Figure 5c. Overall, TEM analysis successfully characterized the nanostructure properties of PANI and PANI/CBTS5, providing essential insights into the potential applications of these materials. In particular, the improved electrical conductivity properties of the PANI/CBTS5 composite, due to the presence of crystalline regions, indicate that it is suitable for use in areas such as energy storage and electronic devices.

The XPS analysis of both pristine PANI nanofibers and PANI nanofibers doped with 5% CBTS chalcogenide material provides valuable insights into the chemical states and composition of these materials, as shown in Figure 6. For the pristine PANI nanofibers, the XPS spectrum prominently displays peaks corresponding to nitrogen (N), carbon (C), and possibly oxygen (O), reflecting the intrinsic chemical structure of the polymer in its nanofiber form (Figure 6a). The N 1s spectrum is particularly significant, offering detailed information on the different nitrogen functionalities within the PANI nanofibers. Typically, the N 1s peak can be deconvoluted into several components: the peak around 399.1 eV corresponds to carbon-nitrogen (C-N). In comparison, the peak at 400.8 eV is associated with amine nitrogen (C=N). Additionally, a peak at higher binding energies (around 402.4 eV) is indicative of protonated amine groups (C=NH<sup>+</sup>), suggesting that the PANI nanofibers are partially protonated, which is characteristic of the emeraldine salt form of the polymer.[33,51,52] This protonation is crucial for the conductivity and electrochemical performance of PANI in its nanofiber structure. The C 1s spectrum typically shows a peak at around 284.3 eV, corresponding to the carbon backbone (C-C and C-H bonds), and additional peaks at higher binding energies (around 285.4-288.1 eV), attributed to carbon-nitrogen bonds (C=O and C=N) in the polymer structure. If oxygen is present, as indicated by the O 1s peak around 530.3–533.1 eV, it could be due to oxidative doping or adsorbed oxygen species, possibly from environmental exposure or the synthesis process. These findings are consistent with the high-resolution transmission electron microscopy (HRTEM) analysis, which confirms the nanofiber morphology and uniformity of PANI.[33,51,52]

In the PANI nanofibers doped with 5% CBTS chalcogenide material, the XPS spectrum reveals the successful incorporation of Cu, Ba, Sn, and S from the CBTS into the PANI matrix, alongside the characteristic peaks of PANI in Figure 6b. The Cu 2p spectrum shows peaks at binding energies of 932.8 and 952.7 eV, corresponding to the Cu  $2p_{3/2}$  and Cu  $2p_{1/2}$  states, respectively, indicating the presence of Cu<sup>+</sup> ions within the composite. The Ba 3d spectrum displays peaks at 780.3 and 795.6 eV, with a splitting energy of 15.3 eV, confirming the presence of Ba<sup>2+</sup> in the material. The Sn 3d peaks, observed at 486.7 and 495.4 eV with a splitting of 8.7 eV, indicate that Sn is present in its tetravalent oxidation state (Sn<sup>4+</sup>).<sup>[26,53]</sup> In the XPS analysis, the S 2p spectrum typically shows characteristic binding energy peaks at 161.8 eV (2p<sub>3/2</sub>) and 163.8 eV (2p<sub>1/2</sub>). However, in the XPS analysis of the PANI/CBTS5 nanofiber composite material, peaks corresponding to thiol (C—S—H), organic disulfides (C-S-S-C), and sulfone (C-SO<sub>2</sub>-C) species, located at 163.8, 164.0, and 168.0 eV, respectively, are observed due to intercalation between carbon and sulfur elements. These peaks provide valuable insight into the sulphur environment within the composite. The presence of (C-SO<sub>2</sub>-C) suggests a degree of surface oxidation occurring during the in situ reaction process, which may impact the material's electrochemical properties. [26,53] This oxidation could influence the conductivity and stability of the material, potentially enhancing the electrochemical reactivity of sulphur and, consequently, the energy storage capacity of the composite. The interaction between the PANI matrix and the CBTS dopant could cause slight shifts in binding energies or alter peak intensities, reflecting potential electronic interactions between the polymer and the chalcogenide. These XPS results align well with the HRTEM analysis, further confirming the successful integration of CBTS within the PANI nanofibers and the uniform distribution of elements within the composite.

Overall, the XPS analysis not only confirms the successful doping of PANI nanofibers with CBTS but also provides a detailed understanding of the chemical states of the constituent elements. This information is crucial for assessing the material's suitability for various applications, particularly in electronic or catalytic devices, where the oxidation states and interactions between different elements can significantly influence performance.

The analysis from Table 2 reveals that PANI exhibits the highest surface area of 35.3 m<sup>2</sup> g<sup>-1</sup>, while the PANI/CBTS20 sample shows the highest cumulative pore volume of  $0.1845 \text{ cm}^3 \text{ g}^{-1}$ . Interestingly, as the ratio of CBTS in the nanocomposite with PANI increases, a notable decrease in the BET surface area is observed. This phenomenon is attributed to the adsorption of CBTS into the pores of PANI, resulting in pore blockage.<sup>[54]</sup> The HK pore volumes in PANI/CBTS composites have increased compared to pure PANI. This can be explained by several factors: (i) Surface Area Reduction: The high surface area of PANI decreases when it is combined with CBTS. The CBTS may block the pore entrances of PANI, resulting in smaller pore sizes. In HK analysis, these smaller pore sizes contribute to higher pore volumes. Material Interactions: The interaction between PANI and CBTS can modify the pore structure, resulting in the formation of smaller pores. Creating micropores (1–2 nm) increases the overall pore volume. (ii) Micropore Formation: Composites tend to develop more micropores compared to macropores. As the dominance of micropores increases, the HK method reports higher pore volumes despite smaller pore sizes. This effect highlights the complex interplay between materials in composite structures and their impact on pore characteristics.<sup>[55,56]</sup> A general review of the literature indicates that the surface area of PANI material is  $\approx 35~\text{m}^2~\text{g}^{-1}$ , and when used in various nanocomposites, this surface area can decrease by up to 50%. This phenomenon is attributed to the pores of the relatively porous PANI material being closed due to the adhesion of the composite materials to the surface. This closure of pores is reported to result in a decrease in both the surface area and cumulative pore volume of PANI nanocomposites. [57,58,19] Moreover, based on the cumulative pore volumes listed in Table 2, it is evident that the pore volume of PANI/CBTS nanocomposite materials is enhanced compared to pure PANI. This increased pore volume is expected to lead to significantly improved electrochemical properties for these nanocomposites, attributed to their larger active surface area.<sup>[59]</sup> Another piece of evidence is that the adsorption and desorption isotherms conform to Type III

23667486, 2025, 10, Downloaded from https://advanced.onlinelibrary.wiley.com/doi/10.1002/adsu.202500427 by Turkey Cochrane Evidence Aid, Wiley Online Library on [02/12/2025]. See the Terms and Conditions

onditions) on Wiley Online Library for rules of use; OA articles are governed by the applicable Creative Commons License

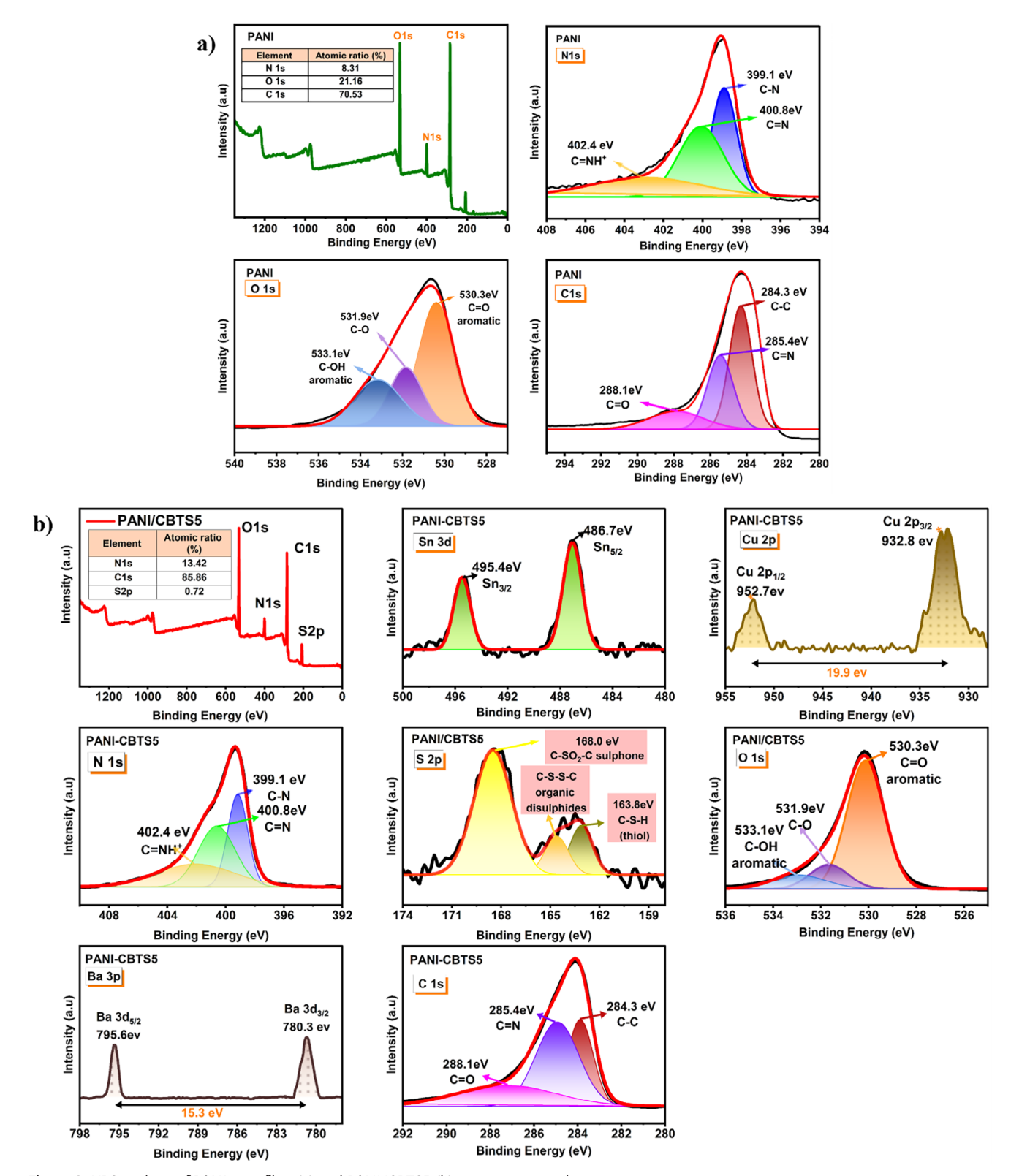


Figure 6. XPS analysis of PANI nanofiber (a) and PANI/CBTS5 (b) composite samples.

onditions) on Wiley Online Library for rules of use; OA articles

governed by the applicable Creative Commons

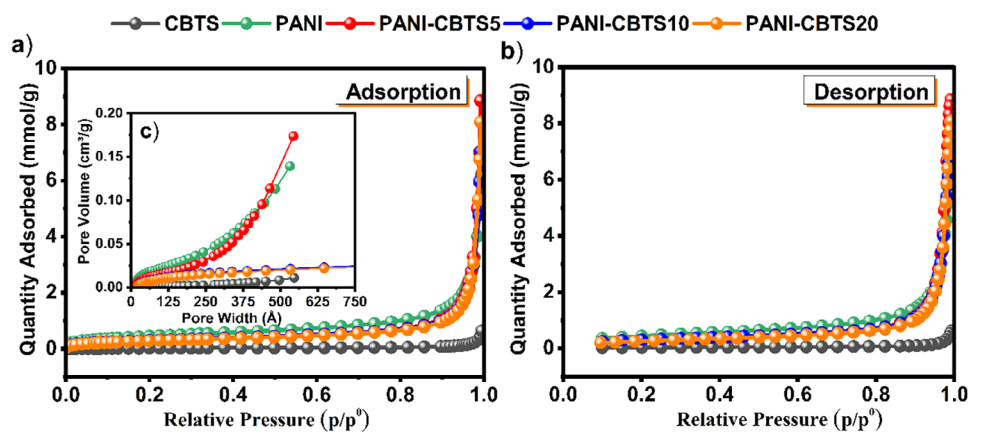


Figure 7. a) Adsorption and b) desorption isotherms and c) pore volume graphs of CBTS, PANI, and PANI/CBTS materials.

adsorption isotherms in the IUPAC classification. Microporous materials exhibiting Type III isotherms tend to adsorb in multiple layers on the material's surface, effectively obstructing the pore surfaces and consequently reducing both pore volume and surface area. [60,61] As seen in Figure 7a,b, the adsorption and desorption isotherms of PANI, CBTS, and PANI/CBTS materials closely resemble the Type III isotherm defined in the IUPAC classification. This similarity strongly suggests that all the synthesized materials possess a microporous structure, with the nanocomposite structures adsorbing onto the material surface in multiple layers. [61]

Table 3 presents a comparative analysis of PANI's surface area, cumulative pore volumes, and those of similar nanocomposites reported in the literature, alongside the results obtained in our study. This comparison reveals that combining PANI with CBTS increases the surface area and cumulative pore volume. This increase is expected to positively influence the electrochemical performance of the nanocomposite. The literature comparison provided in Table 3 reveals that the PANI/CBTS nanocomposite synthesized in our study exhibits a higher surface area and a greater cumulative pore volume compared to many other composites. (Figure S2, Supporting Information)

#### 4. Electrochemical Characterization

The CV tests were conducted on the supercapacitors, designed using synthesized PANI and PANI/CBTS composites with vary-

ing ratios of CBTS as electrodes. The analyses were performed in a two-electrode system, with scan rates ranging from 1 to 200 mV s<sup>-1</sup> and a voltage window of 0–1 V. The electrolyte used was 3 м KOH. The CV curves obtained for each design are displayed in Figure 8. The CV curves of PANI and PANI/CBTS composites exhibited a consistent shape, remaining stable across various scan rates. The consistent shape of the CV curve, irrespective of the difference in scan rate, implies that the electrode material exhibits high cyclic stability.<sup>[68]</sup> Comparing the CV voltammograms of PANI/CBTS designs with those of pure PANI reveals that the oxidation and reduction stages exhibit significantly higher current values. When analyzing the current values at a scan rate of  $50~\text{mV}~\text{s}^{-1}$  in the PANI/CBTS5 sample, a significant difference in current is observed, ≈5 times greater. It is a well-established fact that the area under CV voltammograms is directly correlated with the specific capacitance of the material. This implies that the addition of CBTS enhances the electrochemical characteristics of PANI. However, the CV curves of the designs utilizing pure PANI and PANI/CBTS composites exhibit a nearly rectangular shape, which is characteristic of double-layer capacitor (EDLC) behavior. [69] While the PANI/CBTS composites exhibit a primarily EDLC-based energy storage mechanism, it is essential to note that this behavior is not perfectly ideal, as evidenced by the presence of charge transfer resistance and diffusion limitations observed in the EIS data. The double-layer formation is likely caused by the absorption of K<sup>+</sup> ions (3 M KOH electrolyte) on the surface due to electrode/electrolyte interfacial polarization. [68] There was

Table 3. Comparison of surface area and pore volumes of some PANI-based composites in the literature.

Material	BET surface [m <sup>2</sup> g <sup>-1</sup> ]	Pore volume [cm <sup>3</sup> g <sup>-1</sup> ]	Refs.
PANI-35%CaTiO <sub>3</sub>	13.2	0.049	[62]
PANI/V <sub>2</sub> O <sub>5</sub> /MnO <sub>2</sub>	44.1	0.128	[63]
TiO <sub>2</sub> /MWCNT/PANI	78.7	0.180	[64]
MnSSe-HT-PANI	30.6	0.080	[54]
PANI-MnM	36.0	0.168	[65]
PANI@FePO <sub>4</sub>	15.6	0.124	[66]
Ni <sub>0.5</sub> Zn <sub>0.5</sub> Fe <sub>2</sub> O <sub>4</sub> @PANI	18.4	0.021	[67]
PANI/CBTS5	24.3	0.184	This work*

doi/10.1002/adsu.202500427 by Turkey Cochrane Evidence Aid, Wiley Online Library on [02/12/2025]. See the Terms and Conditions (https://onlinelibrary.wiley.com/terms

and-conditions) on Wiley Online Library for rules of use; OA articles are governed by the applicable Creative Commons License

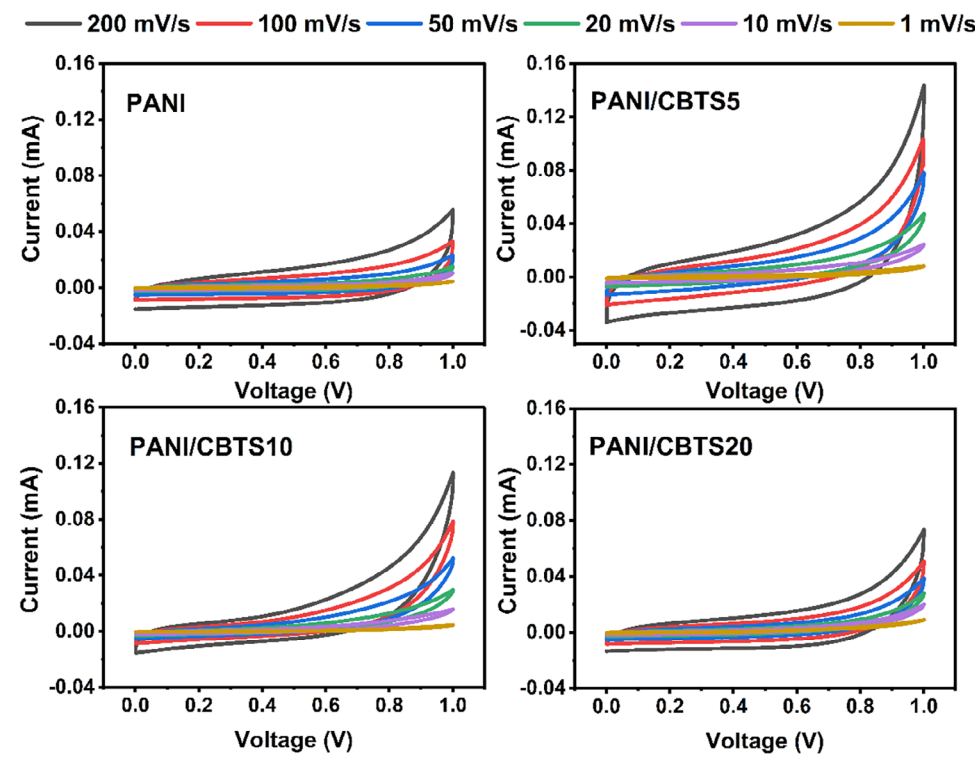
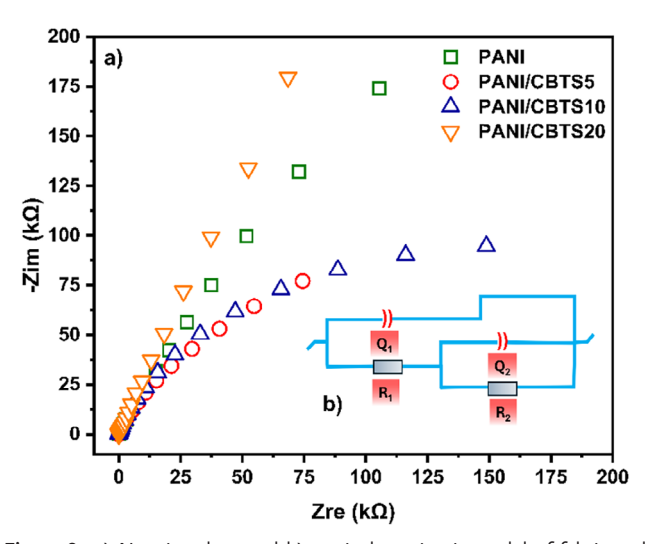


Figure 8. CV curves of prepared supercapacitors produced from PANI and PANI/CBTS compounds.

no occurrence of a redox peak in the CV curve for any of the supercapacitors that were designed.

Impedance measurement is crucial for understanding the electrochemical reactions that occur on the electrode surface and at the electrode/electrolyte interface. [70,71] Nyquist curves are generated through impedance measurement by employing frequencies within a specific range. **Figure 9** illustrates the Nyquist curves of supercapacitor devices utilizing PANI and PANI/CBTS



**Figure 9.** a) Nyquist plots and b) equivalent circuit model of fabricated supercapacitors produced from PANI and PANI/CBTS compounds.

composites as electrodes. Additionally, the Nyquist curves for each supercapacitor design are presented in separate graphs. This combined graph, labelled Figure S3 (Supporting Information), is included in the Supporting Information. By adequately fitting the Nyquist curves with a highly applicable mathematical model, researchers can determine the equivalent circuit model of the supercapacitor device. The equivalent circuit enables a detailed investigation and assessment of both the resistance and reactive components in the whole system. The results represented by circles in Figure 9 are experimental data, while those defined by lines are fitting data. The experimental and fitting data are highly compatible due to the fitting study. Conversely, the  $Z_{\text{re}}$  and  $Z_{\text{im}}$  values (representing the real and imaginary parts, respectively) plotted on the x and y axes of the Nyquist curve correspond to the resistance and reactive elements of the structure. $^{[70,\overline{7}1]}$  Based on the  $Z_{re}$  values, which indicate the resistance component, it is evident that adding 5% CBTS (by mass) to the PANI structure results in a considerable decrease in resistance compared to pure PANI. Nevertheless, it is observed that as the amount of CBTS added increases, the  $Z_{re}$  value increases, and consequently, the resistance also increases. On the other hand, the -Z<sub>im</sub> values, which indicate the reactive elements of impedance (inductance and capacitance), exhibit an analogous behavior to the Z<sub>re</sub> values. Additionally, after a 5% contribution from CBTS, the - $Z_{\rm im}$  values also tend to increase. At a 5% CBTS contribution, the dominant effect is the effect of capacitance rather than inductance. However, as the amount of CBTS increases, the inductance effect becomes more pronounced, resulting in a higher - $Z_{\rm im}$  value. Furthermore, the observed nearly rectangular CV curves, coupled with the EIS data showing charge

www.advancedsciencenews.com



www.advsustains

Table 4. Equivalent circuit parameters of fabricated supercapacitors produced from PANI and PANI/CBTS compounds synthesized using various CBTS as electrodes.

Equiva	lent (	Circuit	[0.	/(R.	$+\Omega_{-}$	/R-\1

Components	PANI	PANI/CBTS5	PANI/CBTS10	PANI/CBTS20	
$R_1$	0.768	0.568	0.67	1.043	
R <sub>2</sub>	299	2281	$3.35 \times 10^{3}$	$44.5 \times 10^{6}$	
$Q_1$	$39.2 \times 10^{-6}$	$50.8 \times 10^{-6}$	$47 \times 10^{-6}$	$51.5 \times 10^{-6}$	
$Q_2$	$0.66 \times 10^{-6}$	$9.81 \times 10^{-6}$	$16.7 \times 10^{-6}$	$33.1 \times 10^{-6}$	
$a_1$	0.76	0.80	0.41	0.56	
$a_2$	0.80	0.24	0.84	0.76	
*** The unit of R is ohm, and	d $Q$ has F.s <sup>(a-1)</sup> .				

transfer resistance and diffusion limitations, consistently indicate that the energy storage mechanism in the PANI/CBTS composites is primarily governed by EDLC behavior.

Table 4 summarizes the components of the equivalent circuit that were obtained through the fitting process. Upon completing the fitting process, it was determined that all designs exhibited identical equivalent circuit models. The values marked as  $R_1$ and  $R_2$  in Table 4 correspond to the electrical resistance resulting from ohmic effects at the interface between the electrode and the electrolyte and the resistance resulting from the double-layer capacitance, respectively. [72]  $Q_1$  represents the capacitance of the double layer, while  $Q_2$  represents the resistance to diffusion.<sup>[73]</sup> As a result of the CBTS incorporation, the ohmic resistance at the interface between the electrode and electrolyte initially decreased and then increased. Thus, when the electrode and electrolyte have more contact, the electrons interact more, reducing the resistance.<sup>[74]</sup> However, when the contribution of CBTS (contact between the electrode and the electrolyte) increases, the contact decreases, and the resistance increases. It is observed that the resistance of the double-layer capacitance increases in line with the contribution of the CBTS. An analogous behaviour is observed in the values of double-layer capacitance,  $Q_1$ . A higher  $R_2$ value indicates that electrochemical reactions experience more excellent resistance or occur at a slower rate across the double layer on the electrode surface. In the PANI/CBTS5 design, there has been an increase in the value of  $Q_2$ . Generally, an increase in Q2 suggests a decrease in the diffusion resistance at the interface between the electrode and the surface or an increase in the effective surface area of the electrode. This indicates that the electrochemical reactions occurring at the interface between the electrode and the material are enhanced. The diffusion resistance is directly proportional to the increase in CBTS contribution. The results are also consistent with Z<sub>re</sub> and -Zim values, and the PANI/CBTS5 design with low ohmic and diffusion resistance is the optimal design based on impedance

Incorporating CBTS into the PANI matrix significantly influenced the charge transfer resistance and, implicitly, the electron transport properties of the resulting nanocomposites. PEIS, particularly the Nyquist plots, revealed a lower charge transfer resistance (R<sub>ct</sub>) for the PANI/CBTS5 composite compared to pristine PANI (Figure 9). This finding suggests that CBTS facilitates faster electron transfer at the electrode-electrolyte interface, contributing to enhanced electrochemical performance. Several factors likely contribute to this improved electron transfer. First, incorporating CBTS appears to enhance the electrical conductivity of the composite, as evidenced by the decrease in ohmic resistance observed in the EIS data. Second, HRTEM images confirmed the presence of well-dispersed CBTS crystalline regions within the PANI matrix (Figure 5). These crystalline regions could act as conductive pathways, facilitating electron transport throughout the composite structure. Third, XPS analysis indicated potential electronic interactions between PANI and CBTS (Figure 6), which could further contribute to the enhanced conductivity and facilitate electron transfer processes. While direct band gap measurements were not conducted in this study, the observed decrease in R<sub>ct</sub>, coupled with the enhanced conductivity and potential electronic interactions, suggests a possible narrowing of the effective band gap in the PANI/CBTS5 composite. A narrower band gap could facilitate more efficient electron transfer under redox conditions, leading to the improved specific capacitance and energy density observed for the PANI/CBTS5 composite compared to PANI.

The supercapacitor design assessment evaluated key parameters, including long-term usability and cycle life. This evaluation was conducted using GCPL to examine the performance of electrodes composed of synthesized PANI and PANI/CBTS composites. The data from the GCPL analysis were obtained under specific conditions, with a current density of 0.1 A g<sup>-1</sup> and after 10000 cycles. To assess the durability of the created supercapacitors, the coulombic efficiency (CE, %) and capacitance retention (CR, %) of all designs were analysed after 10000 cycles. The findings of this analysis are displayed in Figure 10a,b. Consequently, the CE values of all designs exceed 98% even after 10000 cycles, indicating that all designs are suitable for long-term usage. Several examples demonstrated that the CE value partially increased as the number of cycles increased. In contrast, findings comparable to those of the CE analysis were observed when the CR analysis—an indicator of the material's capacitance retention at the end of the charge/discharge period—was investigated (Figure 10b). After 10000 cycles, the design utilizing PANI experienced the greatest decrease in capacitance, whilst the design utilizing PANI/CBTS5 experienced the smallest decrease. Enhancing this parameter could potentially reduce unfavourable side reactions within the system or enhance exceptionally efficient electrochemical reactions.

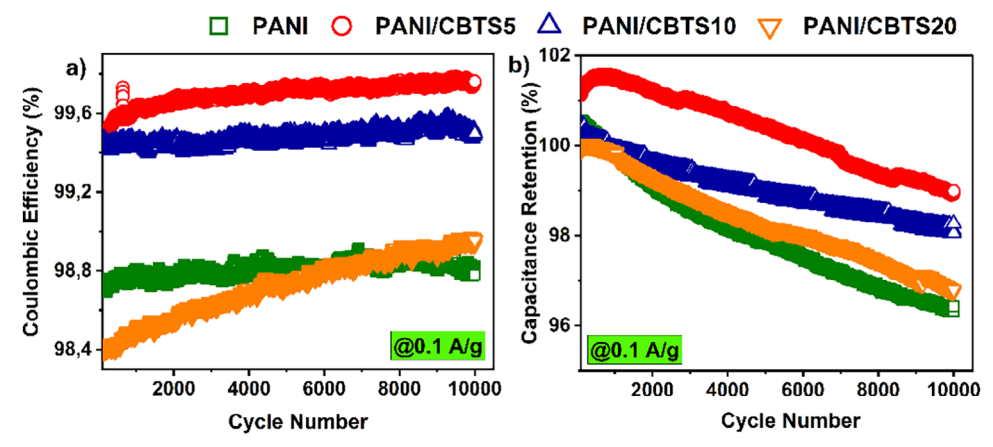


Figure 10. a) coulombic efficiency after 10000 cycles of PANI and PANI/CBTS composites, b) The capacitance retention (%) of all fabricated supercapacitors at  $0.1 \,\mathrm{A \, g^{-1}}$  after 10000 cycles.

The synthesized PANI was doped with varying amounts of CBTS to generate electrode materials in nano form. These materials were then utilized in a two-electrode supercapacitor system. A detailed electrochemical analysis was conducted on the resulting symmetric supercapacitors. The electrochemical parameters obtained are listed in Table 5. Based on the characterization results, the PANI/CBTS5 sample exhibited the highest specific capacitance value, which was determined to be 374.2 F g<sup>-1</sup>. In addition, the energy and power densities were calculated to be 5.2 Wh kg<sup>-1</sup> and 36 kW kg<sup>-1</sup>, respectively. The SEM scans reveal that adding the cauliflower-like form of CBTS to the PANI structure increases thickness. Similarly, the BET analysis shows a decrease in surface area and pore volume as the CBTS ratio rises. A decrease in surface area and pore volume will reduce the amount of active substance in the material, thereby decreasing electrochemical interactions and ultimately decreasing the specific capacitance. The computed values in Table 5 corroborate this outcome. Furthermore, the impedance analysis reveals a significant increase in ohmic resistance following the introduction of 5% CBTS (w/w), resulting in a decline in electrochemical properties. However, like the specific capacitance, energy densities decrease after a 5% contribution of CBTS. This is evident from Figure 10a,b, where the amount of stored energy and the discharge time of the supercapacitor decrease, resulting in a reduction of energy density. Therefore, based on the electrochemical properties, it can be concluded that the most suitable design is PANI/CBTS5.

Therefore, based on the electrochemical properties, it can be concluded that the most suitable design is PANI/CBTS5. The ob-

served maximum at 5% CBTS arises from an optimal balance between enhanced conductivity via well-dispersed CBTS nanocrystals and the preservation of PANI's high surface area for charge storage. At loadings below 5%, CBTS sites are too sparse to form continuous conductive networks, while above 5%, excessive CBTS occludes PANI's porous framework. Although composites with CBTS < 5% were not synthesized here, the clear trend in Table 5 confirms that 5% is the optimum. These results confirm that 5% CBTS is the optimal loading under our conditions.

The electrochemical analysis using Dunn's method, as depicted in Figure 11b,d, reveals that both PANI and PANI/CBTS5 composites exhibit predominantly capacitive behavior, particularly at lower scan rates. However, the incorporation of CBTS significantly enhances the capacitive contribution, aligning with the findings from other electrochemical characterizations. At a scan rate of 1 mV s<sup>-1</sup>, PANI demonstrates a capacitive contribution of  $\approx 20\%$ , with diffusion-controlled processes accounting for the remaining 80%. This suggests that at slower scan rates, the charge storage in PANI is mainly limited by ion diffusion within the bulk of the material. This observation is consistent with the relatively lower specific capacitance and energy density values obtained for PANI in previous electrochemical tests (Figure 11a).

In contrast, the PANI/CBTS5 composite exhibits a capacitive contribution exceeding 95% at the same scan rate, indicating a nearly ideal capacitive behavior (Figure 11c). This observation is in agreement with prior studies on metal chalcogenide–polymer hybrids, where optimized interfacial structures enhanced capacitive contribution at low scan rates.<sup>[75]</sup> This enhancement in capacitive behavior can be attributed to the synergistic effects of CBTS

Table 5. The electrochemical properties of supercapacitors were optimized using PANI and PANI/CBTS compounds, which were synthesized with varying amounts of CBTS as electrodes.

Design	Specific Capacitance [F g <sup>-1</sup> ]	Energy Density [Wh kg <sup>-1</sup> ]	Power Density [kW kg <sup>-1</sup> ]	
PANI	183.2	2.54	27.76	
PANI/CBTS5	374.2	5.20	36.00	
PANI/CBTS10	208.8	2.90	40.15	
PANI/CBTS20	180.0	2.50	28.13	

xonditions) on Wiley Online Library for rules of use; OA articles are governed by the applicable Creative Commons License

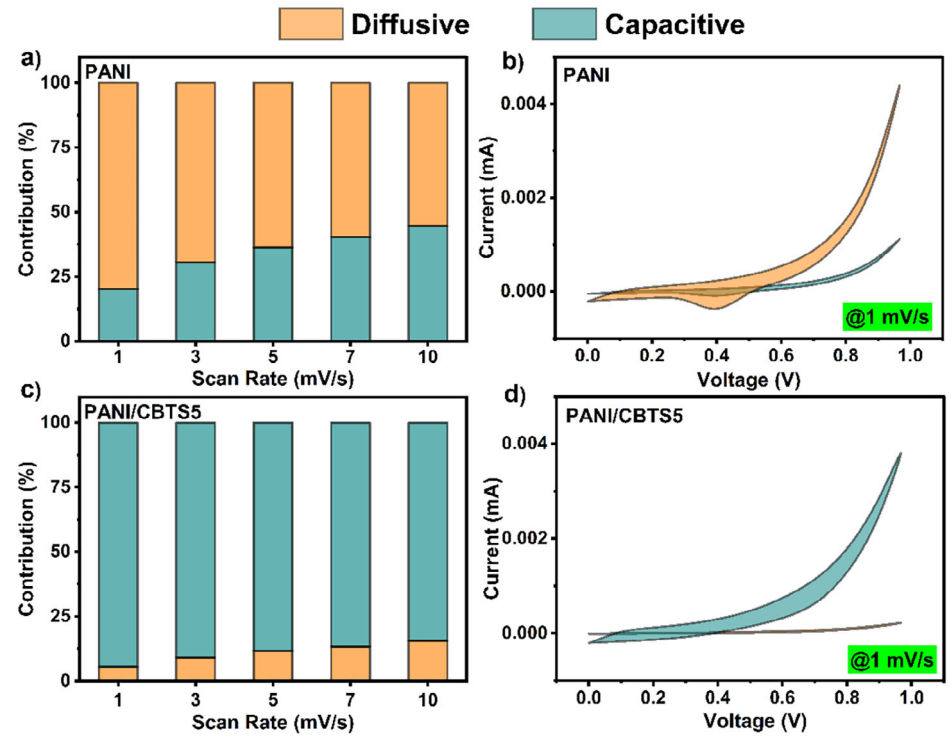


Figure 11. a, c) capacitive and diffusive contributions at different scanning rates and b, d) Capacitive and diffusive regions of the CV curve at 1 mV s<sup>-1</sup>.

incorporation, as evidenced by the improved electrical conductivity, increased surface area, and suppressed diffusion-controlled processes. The enhanced conductivity observed in the impedance analysis facilitates faster electron transport, while the increased surface area, confirmed by BET analysis, provides more active sites for charge accumulation. These factors contribute to the dominance of capacitive charge storage in the PANI/CBTS5 composite, resulting in higher specific capacitance and energy density values compared to pure PANI.

Furthermore, the b-values, derived from the relationship between peak current and scan rate, provide further insights into the charge storage kinetics. The b-value for PANI is 0.65, indicating a mixed capacitive-diffusion controlled behavior, consistent with Dunn's method analysis at low scan rates. However, the b-value for PANI/CBTS5 decreases to 0.43, which is close to the ideal value of 0.5 observed in diffusion-dominated pseudocapacitive systems. This decrease suggests that the incorporation of CBTS enhances faradaic-type intercalation processes while reducing the relative contribution of double-layer capacitance, as also observed in similar metal chalcogenide-based systems.[75,76] This decrease in the b-value suggests that the CBTS incorporation effectively suppresses diffusion-controlled processes, leading to faster charge-discharge kinetics and improved rate capability, which aligns with the superior performance observed for PANI/CBTS5 in the GCPL analysis.

Consequently, the electrochemical analysis using Dunn's method, cyclic voltammetry, and b-value determination reveals that the incorporation of CBTS into the PANI matrix significantly enhances the capacitive contribution to the overall charge storage mechanism. This enhancement, consistent with findings from other electrochemical characterizations, is attributed

to the improved electrical conductivity, increased surface area, and suppressed diffusion-controlled processes, resulting in faster charge—discharge kinetics and improved rate capability, making PANI/CBTS5 a promising material for high-performance supercapacitor applications.

The electrochemical performance of the PANI/CBTS5 composite, as presented in Table 6, highlights its competitive advantage over existing supercapacitor materials. With a specific capacitance of 374.2 F g<sup>-1</sup>, an energy density of 5.20 Wh kg<sup>-1</sup>, and a power density of 36.1 kW kg<sup>-1</sup>, the PANI/CBTS5 composite exceeds numerous materials described in the literature, such as MoS<sub>2</sub>-rGO and NiSe<sub>2</sub>/rGO. These findings demonstrate that the addition of CBTS into the PANI matrix has resulted in considerable gains in both energy and power density while retaining a high specific capacitance. Compared to other materials, the PANI/CBTS5 composite's performance measurements, notably its power density, show that it is a very efficient material for energy storage applications. The comparatively large potential window and the use of 3 M KOH electrolyte further contribute to its exceptional electrochemical performance. These results highlight the potential of CBTS-doped PANI composites as a viable option for enhancing supercapacitor technology. The composite's balance of specific capacitance and energy density, combined with high power density, makes it a suitable contender for future study and development in this sector.

# 5. Applied Potential and Scalability

In addition to advancing scientific knowledge, our work on PANI/CBTS composites looks at real-world applications and scaling issues in energy storage systems. Our study's PANI/CBTS

and-conditions) on Wiley Online Library for rules of use; OA articles are governed by the applicable Creative Commons License



Electrode materials	Potential window [V]	Electrolyte	Specific capacitance $[F g^{-1}]$	Energy density [Wh kg <sup>-1</sup> ]	Power density [kW kg <sup>-1</sup> ]	Refs.
MoS <sub>2</sub> -rGO	-1.0/0	1 M Na <sub>2</sub> SO <sub>4</sub>	329	19.70	1.992	[77]
NiCuCo2S <sub>4</sub>	-0.1/-0.5	3 М КОН	159	35.19	0.66	[78]
CZTS-Z2	0/0.6	3 М КОН	165.04	5.73	3.041	[79]
CuSe/CoSe <sub>2</sub>	-0.3/0.4	3 М КОН	192.8	54.6	0.7	[80]
MnSSe-HT-PANI	-0.2/0.8	3 М КОН	148.4	46.37	15.04	[54]
NiSe <sub>2</sub> /rGO	0/0.45	2 м КОН	333	20.3	_	[81]
CZTS/PANI	-1.0/ 0.4	1 М КОН	371	5.6	1.75	[68]
CZTS/rGO	-0.8/0.4	3 М КОН	248.5	-	_	[5]
$Cu_5Sn_2S_7/ZnS$	0/0.5	6 М КОН	170	9.67	11.08	[82]
PANI/CBTS5	0.0 to 1.0	3 М КОН	374.2	5.20	36.1	This work

composite exhibits potential for various practical energy storage applications. The efficiency and dependability of energy storage systems in renewable energy technologies, electric vehicles, and portable electronics could be significantly enhanced by supercapacitors utilizing PANI/CBTS5. With an energy density of 5.20 Wh kg<sup>-1</sup> and a specific capacitance of 374.2 F g<sup>-1</sup>, this composite is particularly well-suited for applications that require rapid cycles of energy storage and release, such as grid stabilization in renewable energy installations or regenerative braking in automobiles. Scalability is essential for real-world applications.

Our results emphasize the importance of optimizing electrochemical performance while ensuring cost-effectiveness and scalability of manufacturing by adjusting the CBTS concentration to 5%. To fulfill industrial needs and provide consistent performance and dependability across large-scale applications, it will be imperative to scale up manufacturing processes. Resolving scaling issues requires not only improving synthesis methods but also ensuring that supply chains are stable and that regulations are followed to enable broad adoption.

By reducing dependency on conventional fossil fuel-based energy sources, PANI/CBTS composites enhance performance and promote environmental sustainability in energy storage systems. This shift facilitates global efforts to reduce greenhouse gas emissions and combat climate change. Furthermore, the economic ramifications are noteworthy, as the competitiveness of PANI/CBTS composites in the energy storage market depends on their long-term durability and cost-effectiveness. Our research concludes by outlining the potential real-world applications and scaling concerns of PANI/CBTS composites while also highlighting their scientific achievements. To overcome scaling issues and optimize these composites for broad commercial use, further research and development are essential. This will hasten the shift to sustainable energy alternatives.

# 6. Conclusion

In this study, we synthesized and evaluated nanofiber PANI and PANI/CBTS composites (5%, 10%, and 20% CBTS by weight) as electrode materials for supercapacitor applications. Comprehensive structural and electrochemical characterizations revealed that the incorporation of CBTS significantly influenced the morphology, porosity, and performance of the composites.

Despite a decrease in BET surface area and pore volume upon CBTS addition, the PANI/CBTS5 composite exhibited the highest electrochemical performance, achieving a specific capacitance of 374.2 F g<sup>-1</sup>, energy density of 5.20 Wh kg<sup>-1</sup>, and over 92% cycling stability after 10,000 cycles. HRTEM confirmed the formation of well-dispersed CBTS crystalline domains (12–26 nm) on PANI nanofibers (40–60 nm), while XPS analysis revealed strong chemical interactions between PANI and CBTS elements (Cu, Ba, Sn, S), supporting improved charge transport.

Electrochemical impedance spectroscopy demonstrated reduced charge transfer resistance in PANI/CBTS5 compared to pure PANI, corroborating enhanced conductivity. Dunn's analysis further confirmed the dominant capacitive behavior of PANI/CBTS5 at low scan rates.

These results demonstrate that CBTS incorporation into PANI creates a synergistic interface that enhances conductivity, structural stability, and charge storage capability. Among the tested compositions, 5% CBTS loading provides the optimal balance, making PANI/CBTS5 a promising electrode candidate for next-generation supercapacitors.

This work opens a new pathway for engineering polyanilinebased hybrid electrodes with chalcogenide semiconductors, offering practical advantages for high-performance and durable energy storage systems.

#### **Supporting Information**

Supporting Information is available from the Wiley Online Library or from the author.

# **Acknowledgements**

This study was supported by the Scientific and Technological Research Council of Turkey (TUBITAK) under Grant Numbers 123M826 and 121C416. The authors thank TUBITAK for their support.

# **Conflict of Interest**

The authors declare no conflict of interest.

23667486, 2025, 10, Downloaded from https://advanced.onlinelibrary.wiley.com/doi/10.1002/adsu.202500427 by Turkey Cochrane Evidence Aid, Wiley Online Library on [02/12/2025]. See the Terms

on Wiley Online Library for rules of use; OA articles are governed by the applicable Creative Commons



## **Author Contributions**

S.G.C. planned and designed the synthesis and modification of CBTS and performed the experiments related to the synthesis of CBTS. S.G.C., U.B.S., and M.O.A.C. collected and analyzed the data. A.G. and S.G.C. planned and designed the use as electrode materials in supercapacitors. A.G. planned and designed EPR and EIS studies. E.E. and A.G. produced the supercapacitor. E.E. collected and analyzed the data. The manuscript was written with contributions from S.G.C., A.G., M.O.A.C., U.B.S., R.G.A., and E.E. All authors take full responsibility for the paper's content and have approved the final version of the manuscript.

# **Data Availability Statement**

The data that support the findings of this study are available from the corresponding author upon reasonable request.

## **Keywords**

 $\text{Cu}_2\text{BaSnS}_4$ , nanofiber composites, polyaniline, supercapacitors, surface area

Received: April 9, 2025 Revised: July 23, 2025 Published online: August 4, 2025

- [1] S. Kumar, G. Saeed, L. Zhu, K. N. Hui, N. H. Kim, J. H. Lee, *Chem. Eng. J.* 2021, 403, 126352.
- [2] T. Chen, M. Li, Y. Li, S. Song, J. Kim, J. Bae, Mater. Sci. Eng., B 2023, 290, 116354.
- [3] C. Lu, X. Chen, Acc. Chem. Res. 2020, 53, 1468.
- [4] J. Huang, Y. Xie, Y. You, J. Yuan, Q. Xu, H. Xie, Y. Chen, Adv. Funct. Mater. 2023, 33, 2213095.
- [5] Q. Tang, H. Shen, H. Yao, W. Wang, Y. Jiang, C. Zheng, Ceram. Int. 2016, 42, 10452.
- [6] A. Güngör, S. G. Çolak, M. Ö. Alaş Çolak, R. Genç, E. Erdem, Electrochim. Acta 2024, 480, 143924.
- [7] S. Yuan, S. Wang, L. Li, Y. H. Zhu, X. B. Zhang, J. M. Yan, ACS Appl. Mater. Interfaces 2016, 8, 9178.
- [8] M. Isacfranklin, R. Yuvakkumar, G. Ravi, D. Velauthapillai, Mater. Adv. 2022. 3, 6643.
- [9] M. Isacfranklin, R. Yuvakkumar, G. Ravi, B. Saravanakumar, M. Pannipara, A. G. Al-Sehemi, D. Velauthapillai, ACS Omega 2021, 6, 9471
- [10] K. Y. Hameed, B. Faisal, T. Hanae, S. B. Marí, B. Saira, K. N. A. Kaim, Bull. Mater. Sci. 2019, 42, 1.
- [11] A. K. Patel, R. Mishra, S. K. Soni, Semicond. Sci. Technol. 2024, 39, 015005.
- [12] Y. H. Khattak, F. Baig, H. Toura, S. Beg, B. M. Soucase, J. Mater. Sci. 2019, 54, 14787.
- [13] J. Jiang, Y. Qiu, H. Dong, L. Yang, Y. Miao, L. Xiong, B. Gao, X. Zhang, P. K. Chu, X. Peng, J. Colloid Interface Sci. 2025, 686, 681.
- [14] H. Fu, Y. Chen, Y. Yang, N. Zhou, J. Dai, D. Li, Q. Luo, X. Wang, R. Jia, H. Ren, Q. Qin, Y. Xu, L. Dai, *Inorg. Chem. Front.* 2025, 12, 4653.
- [15] G. A. Snook, P. Kao, A. S. Best, J. Power Sources 2011, 196, 1.
- [16] Y. Zhao, B. Liu, L. Pan, G. Yu, Energy Environ. Sci. 2013, 6, 2856.
- [17] S. Bhadra, D. Khastgir, N. K. Singha, J. H. Lee, Prog. Polym. Sci. 2009, 34, 783.
- [18] M. Jaymand, Prog. Polym. Sci. 2013, 38, 1287.
- [19] E. Shanmugasundaram, V. Ganesan, V. Narayanan, K. Vellaisamy, N. Saleh, S. Thambusamy, *Nanoscale Adv.* **2024**, *6*, 1765.

- [20] M. B. Gholivand, H. Heydari, A. Abdolmaleki, H. Hosseini, Mater. Sci. Semicond. Process. 2015, 30, 157.
- [21] T. Liu, L. Finn, M. Yu, H. Wang, T. Zhai, X. Lu, Y. Tong, Y. Li, Nano Lett. 2014, 14, 2522.
- [22] S. Shaheen Shah, S. Oladepo, M. Ali Ehsan, W. Iali, A. Alenaizan, M. Nahid Siddiqui, M. Oyama, A. R. Al-Betar, M. A. Aziz, *Chem. Rec.* 2024, 24, 202300105.
- [23] R. Vinodh, R. S. Babu, S. Sambasivam, C. V. V. Muralee Gopi, S. Alzahmi, H. J. Kim, A. L. F. de Barros, I. M. Obaidat, *Nanomaterials* 2022, 12, 1511.
- [24] A. Güngör, S. G. Çolak, M. Ö. Alaş Çolak, R. Genç, E. Erdem, Electrochim. Acta 2024, 480, 143924.
- [25] S. Levcenko, B. Teymur, D. B. Mitzi, T. Unold, APL Mater. 2021, 9, 111108.
- [26] A. Ali, S. Ahmed, J. ur Rehman, M. R. Abdullah, H. Bin Chen, B. Guo, Y. Yang, Mater Today Commun. 2021, 26, 101675.
- [27] M. S. Kumar, S. P. Madhusudanan, S. K. Batabyal, *Mater. Charact.* 2021, 174, 110988.
- [28] N. R. Chiou, L. J. Lee, A. J. Epstein, J. Mater. Chem. 2008, 18, 2085.
- [29] A. M. Afzal, N. Muzaffar, M. W. Iqbal, G. Dastgeer, A. Manzoor, M. Razaq, S. M. Wabaidur, E. A. Al-Ammar, S. M. Eldin, J. Appl. Electrochem. 2024, 54, 65.
- [30] P. Simon, Y. Gogotsi, Nat. Mater. 2008, 7, 845.
- [31] M. Z. Iqbal, M. M. Faisal, M. Sulman, S. R. Ali, A. M. Afzal, M. A. Kamran, T. Alharbi, J. Energy Storage 2020, 29, 101324.
- [32] T. Schoetz, L. W. Gordon, S. Ivanov, A. Bund, D. Mandler, R. J. Messinger, Electrochim. Acta 2022, 412, 140072.
- [33] A. H. Majeed, L. A. Mohammed, O. G. Hammoodi, S. Sehgal, M. A. Alheety, K. K. Saxena, S. A. Dadoosh, I. K. Mohammed, M. M. Jasim, N. U. Salmaan, *Int. J. Polym. Sci.* 2022, 2022, 9047554.
- [34] Z. Ergönenç Yavas, D. Cevher, H. T. Silis, A. Cirpan, O. Gülseren, C. Franchini, J. Phys. Chem. C 2023, 127, 6813.
- [35] O. P. Dimitriev, Macromolecules 2004, 37, 3388.
- [36] O. P. Dimitriev, Synth. Met. 2004, 142, 299.
- [37] Md. Saddam Hossain, Appl. Chem. 2019, 2, 1.
- [38] A. M. Mengesha, International of Journal of Bioorganic Chemistry **2022**, *7*, 1.
- [39] A. Güngör, F. Bakan-Misirlioglu, R. Genç Alturk, E. Erdem, J. Energy Storage 2024, 76, 110143.
- [40] K. K. Pandey, J. Appl. Polym. Sci. 1999, 71, 1969.
- [41] S. X. Zhou, X. Y. Tao, J. Ma, L. T. Guo, Y. B. Zhu, H. L. Fan, Z. S. Liu, X. Y. Wei. Vacuum 2018, 149, 175.
- [42] H. Yu, Q. Guo, C. Wang, G. Cao, Y. Liu, Prog. Org. Coat. 2023, 182, 107611.
- [43] H. Wang, J. Lin, Z. Xiang, J. Sci.: Adv. Mater. Dev. 2016, 1, 225.
- [44] P. Saini, V. Choudhary, B. P. Singh, R. B. Mathur, S. K. Dhawan, *Mater. Chem. Phys.* 2009, 113, 919.
- [45] M. V. Gapanovich, V. V. Rakitin, G. F. Novikov, Russ. J. Inorg. Chem. 2022, 67, 1.
- [46] Z. Chen, K. Sun, Z. Su, F. Liu, D. Tang, H. Xiao, L. Shi, L. Jiang, X. Hao, Y. Lai, ACS Appl. Energy Mater. 2018, 1, 3420.
- [47] A. Crovetto, Z. Xing, M. Fischer, R. Nielsen, C. N. Savory, T. Rindzevicius, N. Stenger, D. O. Scanlon, I. Chorkendorff, P. C. K. Vesborg, ACS Appl. Mater. Interfaces 2020, 12, 50446.
- [48] B. Teymur, Y. Zhou, E. Ngaboyamahina, J. T. Glass, D. B. Mitzi, Chem. Mater. 2018, 30, 6116.
- [49] R. Chakraborty, K. M. Sim, M. Shrivastava, K. V. Adarsh, D. S. Chung, A. Nag, ACS Appl. Energy Mater. 2019, 2, 3049.
- [50] K. Mahmood, M. Imran, M. Hameed, F. Rehman, S. W. Ahmad, F. Nawaz, Nanoscale Adv. 2019, 1, 2167.
- [51] S. Bhandari, in Polyaniline Blends, Composites, and Nanocomposites, Elsevier, Amsterdam, The Netherlands, 2018, Ch.2.
- [52] K. Wu, P. Fu, Z. Wang, Q. Zhao, J. Guo, B. Ruan, M. Wu, Polym. Adv. Technol. 2021, 32, 2082.

ADVANCED Sustainable Systems

www.advancedsciencenews.com

www.advsustainsys.com

- [53] P. M. S. Banu, J. Henry, G. Sivakumar, K. Prabakar, K. Mohanraj, New J. Chem. 2023, 47, 18555.
- [54] K. Y. Yasoda, M. Afshan, S. C. Caroline, E. M. Harini, K. Ghosh, S. K. Batabyal, *Electrochim. Acta* 2024, 117, 480.
- [55] T. Guo, Y. Zhang, J. Chen, W. Liu, Y. Geng, A. H. Bedane, Y. Du, Case Stud. Therm. Eng. 2024, 53, 103925.
- [56] R. J. Dombrowski, C. M. Lastoskie, D. R. Hyduke, Colloids Surf. A: Physicochem. Eng. Asp. 2001, 187, 23.
- [57] G. Joseph, S. D. Kalathiparambil Rajendra Pai, A. Varghese, D. Pinheiro, M. K. Mohan, S. J. Chundattu, J. Mol. Struct. 2024, 1308, 138095
- [58] H. Jia, H. Xu, M. Shi, Y. Yan, K. Lu, M. Xia, F. Wang, Sep. Purif. Technol. 2023, 325, 124652.
- [59] D. A. Tonpe, K. P. Gattu, V. V. Kutwade, S. H. Han, B. R. Sathe, R. Sharma, J. Energy Storage 2024, 81, 110434.
- [60] M. Khosya, D. Kumar, M. Faraz, N. Khare, Int. J. Hydrogen Energy 2023, 48, 2518.
- [61] M. Hasanzadeh, R. Ansari, M. Farahpour, Synth. Met. 2024, 302, 117549.
- [62] A. Bibi, A. Shakoor, M. Raffi, M. Hina, N. A. Niaz, S. A. Fatima, M. N. Qureshi, J. Energy Storage 2024, 78, 110321.
- [63] A. Varghese, S. Devi K R, D. Pinheiro, M. K. Mohan, Surf. Interfaces 2023, 41, 110321.
- [64] M. Karamifar, S. Sabbaghi, M. S. Mohtaram, K. Rasouli, M. Mohsenzadeh, H. Kamyab, A. Derakhshandeh, L. Dolatshah, H. Moradi, S. Chelliapan, *Powder Technol.* 2024, 432, 119176.
- [65] I. Izwan Misnon, R. Jose, Mater. Today Proc. 2020, 41, 513.
- [66] A. Waghmare, R. Rathore, A. Pandey, V. Chandra, Mater. Sci. Eng.: B 2024, 302, 117253.
- [67] R. Tanwar, B. Kaur, U. Kumar Mandal, Appl. Catal. B 2017, 211, 305.

- [68] C. Sabanhalli, K. Roy, M. P. Kumar, R. Mudike, A. K. C. S, P. D. Shivaramu, K. G. B. Kumar, N. Basavegowda, D. Rangappa, Ceram. Int. 2022, 48, 35860.
- [69] P. Tiwari, J. Jaiswal, R. Chandra, Electrochim. Acta 2019, 324, 134767.
- [70] R. Srinivasan, F. Fasmin, in An Introduction to Electrochemical Impedance Spectroscopy, CRS Press, Boca Raton, FL, USA 2021.
- [71] V. Vivier, M. E. Orazem, Chem. Rev. 2022, 122, 11131.
- [72] D. Sanchez-Herrera, D. Pacheco-Catalan, R. Valdez-Ojeda, B. Canto-Canche, X. Dominguez-Benetton, J. Domínguez-Maldonado, L. Alzate-Gaviria, BMC Biotechnol. 2014, 14, 1.
- [73] A. M. Fenelon, C. B. Breslin, J. Appl. Electrochem. 2001, 31, 509.
- [74] R. Li, /Chemcomm, L. Zhao, F. Ran, Chem. Commun. 2023, 59, 6969.
- [75] C. Du, X. Cheng, B. Lu, W. Zhou, J. Zhang, J. Xu, G. Zhang, G. Nie, Energy Storage Mater. 2025, 80, 104394.
- [76] C. Du, H. Li, G. Zhang, R. Wan, W. Zhang, X. Xu, L. Zheng, X. Deng, J. Xu, B. Lu, G. Nie, Chem. Eng. J. 2024, 495, 153692.
- [77] A. M. Zardkhoshoui, S. S. H. Davarani, J. Electroanal. Chem. 2018, 827, 221.
- [78] S. K. Shinde, H. M. Yadav, G. S. Ghodake, A. D. Jagadale, M. B. Jalak, D. Y. Kim, *Ceram. Int.* 2021, 47, 15639.
- [79] A. Murugan, V. Siva, A. samad Shameem, S. A. Bahadur, J. Energy Storage 2021, 44, 103423.
- [80] K. Karuppasamy, D. Vikraman, S. Hussain, G. Kumar Veerasubramani, P. Santhoshkumar, S. H. Lee, R. Bose, A. Kathalingam, H. S. Kim, Chem. Eng. J. 2022, 427, 131535.
- [81] M. Lu, M. Y. Sun, X. H. Guan, X. M. Chen, G. S. Wang, RSC Adv. 2021, 11, 11786.
- [82] F. Yu, V. T. Tiong, L. Pang, R. Zhou, X. Wang, E. R. Waclawik, K. (Ken) Ostrikov, H. Wang, Chin. Chem. Lett. 2019, 30, 1115.